

Development of non-pyrogenic magnetosome minerals coated with poly- l -lysine leading to full disappearance of intracranial U87-Luc tumors in 100% of treated mice using magnetic hyperthermia

Edouard Alphandéry, Ahmed Idbaih, Clovis Adam, Jean-Yves Delattre, Charlotte Schmitt, François Guyot, Imène Chebbi

▶ **To cite this version:**

Edouard Alphandéry, Ahmed Idbaih, Clovis Adam, Jean-Yves Delattre, Charlotte Schmitt, et al.. Development of non-pyrogenic magnetosome minerals coated with poly- l -lysine leading to full disappearance of intracranial U87-Luc tumors in 100% of treated mice using magnetic hyperthermia. Biomaterials, 2017, 141, pp.210-222. 10.1016/j.biomaterials.2017.06.026 . hal-01545933

HAL Id: hal-01545933

https://hal.sorbonne-universite.fr/hal-01545933

Submitted on 23 Jun 2017

HAL is a multi-disciplinary open access archive for the deposit and dissemination of scientific research documents, whether they are published or not. The documents may come from teaching and research institutions in France or abroad, or from public or private research centers.

L'archive ouverte pluridisciplinaire **HAL**, est destinée au dépôt et à la diffusion de documents scientifiques de niveau recherche, publiés ou non, émanant des établissements d'enseignement et de recherche français ou étrangers, des laboratoires publics ou privés.

ACCEPTED MANUSCRIPT

Development of non-pyrogenic magnetosome minerals coated with poly-L-lysine leading to full disappearance of intracranial U87-Luc tumors in 100% of treated mice using magnetic hyperthermia.

Edouard Alphandéry [1,2(*)], Ahmed Idbaih [3,4], Clovis Adam [5], Jean-Yves Delattre [3,4], Charlotte Schmitt [3], François Guyot [1] and Imène Chebbi [2]

[1] Institut de minéralogie de physique des matériaux et de cosmochimie, UMR 7590 CNRS, Sorbonne Universités, UPMC, University Paris 06, Muséum National d'Histoire Naturelle, 4 Place Jussieu, 75005, Paris, France.

[2] Nanobacterie SARL, 36 boulevard Flandrin, 75016, Paris, France.

[3] Inserm U 1127, CNRS UMR 7225, Sorbonne Universités, UPMC Univ Paris 06 UMR S 1127, Institut du Cerveau et de la Moelle épinière, ICM, F-75013, Paris, France

[4] AP-HP, Hôpitaux Universitaires La Pitié Salpêtrière - Charles Foix, Service de Neurologie 2-Mazarin, F-75013, Paris, France.

[5] Laboratoire de neuropathologie, GHU Paris-Sud-Hôpital Bicêtre, 78 rue du Général Leclerc, 94270 Le Kremlin Bicêtre, France.

*CORRESPONDING AUTHOR EMAIL ADDRESS: edouardalphandery@hotmail.com

ACCEPTED MANUSCRIPT

ABSTRACT

Magnetic hyperthermia was reported to increase the survival of patients with recurrent glioblastoma by 7 months. This promising result may potentially be further improved by using iron oxide nanoparticles, called magnetosomes, which are synthesized by magnetotactic bacteria, extracted from these bacteria, purified to remove most endotoxins and organic material, and then coated with poly-L-lysine to yield a stable and non-pyrogenic nanoparticle suspension. Due to their ferrimagnetic behavior, high crystallinity and chain arrangement, these magnetosomes coated with poly-L-lysine (M-PLL) are characterized by a higher heating power than their chemically synthesized counterparts currently used in clinical trials. M-PLL-enhanced antitumor efficacy was demonstrated by administering 500 to 700 µg in iron of M-PLL to intracranial U87-Luc tumors of 1.5 mm^3 and by exposing mice to 27 magnetic sessions each lasting 30 minutes, during which an alternating magnetic field of 202 kHz and 27 mT was applied. Treatment conditions were adjusted to reach a typical hyperthermia temperature of 42 °C during the first magnetic session. In 100% of treated mice, bioluminescence due to living glioblastoma cells fully disappeared 68 days following tumor cell implantation (D68). These mice were all still alive at D350. Histological analysis of their brain tissues revealed an absence of tumor cells, suggesting that they were fully cured. In comparison, antitumor efficacy was less pronounced in mice treated by the administration of IONP followed by 23 magnetic sessions, leading to full tumor bioluminescence disappearance in only 20% of the treated mice.

KEYWORDS

Magnetosomes, magnetotactic bacteria, magnetic hyperthermia, alternating magnetic field, glioblastoma, U87, magnetic hyperthermia.

ACCEPTED MANUSCRIPT

1. INTRODUCTION

Every year, 25,000 patients in the United States and in Europe are diagnosed with glioblastoma (GBM) [1, 2], a dreadful disease with a low 5-year survival rate of 10% with standard treatments [3, 4]. New treatments are under development to improve this poor prognosis [5-13]. Among them, different types of thermotherapies such as whole-body hyperthermia, ultrasound waves, radiofrequency microwaves, phototherapy and magnetic hyperthermia have been tested [14]. Compared with other thermotherapies, magnetic hyperthermia treatment [5-20], in which iron oxide nanoparticles are administered to tumors and heated under alternating magnetic field (AMF) application, requires lower heating temperatures of 43-50 °C to be efficient. This is due to a more localized heat that improves efficacy and safety. Using chemical superparamagnetic iron oxide nanoparticles (SPION), the magnetic hyperthermia treatment of patients with GBM was associated with an increase in patient survival following the diagnosis of first tumor recurrence of 7 months compared with conventional therapies [4, 21, 22]. To improve further the efficacy of magnetic hyperthermia, magnetic nanoparticles with better heating properties than those of SPION could be used. Such properties may be achieved by stable magnetic single domain iron oxide nanoparticles, which are either doped with cobalt to increase magnetocrystalline anisotropy [23], or that possess a large size, typically between 40 and 100 nm, leading to ferrimagnetic properties.

In this article, instead of introducing a toxic compound such as cobalt in nanoparticles, we use magnetotactic bacteria to synthesize large nanominerals called magnetosomes. The latter are cubo-octahedric iron oxide minerals composed of magnetite or maghemite depending on their level of oxidation, which are surrounded by biological material and usually organized in chains. Compared with SPION, magnetosomes are larger and better crystallized, yielding improved magnetic properties useful in a series of different applications, including magnetic hyperthermia [24]. In addition, due to their chain arrangement, magnetosomes are not prone to aggregation and lead to homogenous tumor temperature distribution [25-30]. In previous studies, suspensions of chains of magnetosomes isolated from magnetotactic bacteria were administered to MDA-MB-231 breast tumors xeno-grafted subcutaneously

under the skin of mice and were exposed to several AMF applications, yielding more efficient antitumor efficacy than SPION [25, 26]. Despite these appealing features, magnetosomes suffer from two drawbacks that have hindered their industrial development. On the one hand, the biological material surrounding their mineral core is difficult to fully characterize and obtain reproducibly with the same composition. In addition, in the absence of a specific treatment, they contain lipopolysaccharide since magnetosomes originate from gram-negative magnetotactic bacteria. On the other hand, with most current methods of bacterial growth, magnetosome production yield is relatively low, typically below 10 mg/L/day [31].

In this study, we have developed a magnetosome synthesis method that uses MSR-1 magnetotactic bacteria and leads to a large amount of magnetosomes (~100 mg per liter of growth medium). In this method, magnetosomes were first isolated from magnetotactic bacteria, most biological material was removed, and the magnetosome mineral core was then stabilized with a poly-L-lysine coating, leading to nanoparticles called M-PLL. M-PLL properties such as composition, surface charge, magnetic parameters, stability, cytoxicity, pyrogenicity, and systemic and brain toxicity, were determined and compared with those of chemically synthesized iron oxide nanoparticles (IONP) currently used for magnetic hyperthermia [32, 33]. Then, we studied in vitro whether M-PLL and IONP induce U87-Luc cell death in the presence (or not) of an AMF and whether cell death occurs through an apoptotic or necrotic mechanism.

The anti-tumor efficacy of M-PLL and IONP was also examined in vivo by first growing U87-Luc human GBM tumor cells inside the brain of nude mice. When tumors reached a size of ~ 1.5 mm^3, 2 µl of a suspension containing 500 µg in iron of M-PLL or IONP was administered at the site of tumor cell implantation and mice were then exposed 23 or 27 times for 30 minutes to an AMF of strength 27 mT and frequency 202 kHz. When the tumors re-grew despite the magnetic treatments, we re-administered 200 µg in iron of M-PLL or IONP at 47 days following tumor cell implantation (D47). To compare the efficacy of both treatments, the maximum mouse survival day reached with M-PLL and IONP was

estimated. Possible mechanisms responsible for antitumor activity were also examined and we distinguished between those taking place in heated and unheated regions.

2. MATERIALS AND METHODS

2.1. Classification of the different suspensions of nanoparticles as a medical device of class III

Suspensions containing IONP and M-PLL were classified as medical devices of class III, since medical products containing nanomaterials, which were also activated by an external source of energy and used to treat cancer, were categorized as such [34, 35].

2.2. Preparation of the M-PLL suspension

2.1.1. Growth of MSR-1 magnetotactic bacteria

MSR-1 magnetotactic bacteria were purchased from DSMZ (DSM-6361, Braunschweig, Germany). After cultivation in an agar gel, several colonies of these bacteria were collected and amplified in a pre-culture growth medium without iron up to an optical density measured at 565 nm (OD_{565}) of ~ 0.5-2. Cells were then grown in a fermenter under batch fed conditions using an acid solution containing an iron source that maintained the pH of the growth medium at 6.9. During fermentation, oxygen was bubbled in the growth medium with an air compressor to promote bacterial growth while maintaining oxygen concentration below 0.1% to enable magnetosome synthesis. After 75 hours, we obtained a bacterial suspension with OD_{565} ~ 10-12 containing ~100 mg of magnetosomes in iron per liter of growth medium, as deduced by the iron assay. The growth protocol of magnetotactic bacteria is detailed in the supplementary information (SI).

2.1.2. Preparation of uncoated magnetosome minerals, M-Uncoated

Following fermentation, suspensions of bacteria were concentrated and re-suspended successively in several solvents (1 M NaOH, 1X PBS, Triton X-100 and 1% SDS, phenol, chloroform) under different sonication and temperature conditions and for various times to remove most organic material originating from the magnetotactic bacteria. The resulting suspension contained mainly the

mineral cores of the magnetosomes. The suspension was autoclaved for sterilization. The method used to prepare suspensions of M-Uncoated is detailed in SI.

2.1.3. Preparation of suspensions of magnetosome minerals coated with poly-L-lysine, M-PLL

Suspensions of M-Uncoated at 20 mg/mL in iron were mixed under sterile conditions with a poly-L-lysine solution at 40 mg/mL at pH 9.5 under sonication. The supernatant containing free poly-L-lysine in excess was removed. Nanoparticle suspensions were washed with sterile water. Water was removed and replaced with 5% glucose. A sterile and injectable suspension of M-PLL mixed in 5% of glucose was thus obtained. The method used to prepare suspensions of M-PLL is detailed in SI.

2.3. Preparation of the IONP suspension

Ferrimagnetic chemically synthesized iron oxide nanoparticles (IONP) were purchased from Micromod, reference: 10-00-102 [33]. Prior to their administration in mice and to *in vitro* studies, IONP suspensions were centrifuged at 14,000 rpm (12x4 g) for 30 min and were then washed 3 times with a sterile injectable solution of 5% glucose.

2.4. Measurements on the different suspensions

To measure iron concentrations, nanoparticle sizes, morphology, surface charge, stability, surface and core composition, and magnetic properties, we used a series of different methods based on optical absorption, transmission electron microscopy, dynamic light scattering, Fourier transform infrared (FT-IR), carbon, hydrogen, nitrogen, and sulfur (CHNS) elemental analysis, or vibrating sample magnetometry (VSM), as described in more detail in SI.

2.5. Toxicity assessment of the suspensions of nanoparticles

In vitro cytotoxicity of M-PLL and IONP in healthy cells was evaluated by a neutral red uptake assay (NRU). In this assay, various nanoparticle concentrations (between 16 µg/mL and 1 mg/mL in iron) were incubated with 3T3 cells for 24 hours, and the percentage of cell inhibition was measured by optical absorbance. A non-cytotoxic behavior corresponded to a percentage of inhibition, which was

below 30%. We used a nanoparticle concentration that varied between the nanoparticle concentration of 6 cm^2/mL, corresponding to 22 µg/mL, and the nanoparticle concentration of 1 mg/mL necessary to heat cells *in vitro* (see section 2.7). The endotoxin concentration of the M-PLL and IONP suspensions was measured by a Limulus Amebocyte Lysate (LAL) assay and the pyrogenicity of these suspensions was evaluated by a rabbit test.

Acute systemic toxicity of IONP and M-PLL was examined by intravenously injecting 100 µL of nanoparticle suspensions at a concentration of 50 mg in iron per ml in the tails of 6-week-old C57/BL6 mouse females. The brain toxicity of IONP and M-PLL was studied by injecting at brain coordinate (0.2.2) mm different concentrations in iron of M-PLL and IONP (250, 100, 50 and 20 mg/mL in iron) in the right hemisphere of 5-week-old athymic female nude mice. To evaluate systemic and brain toxicities, the mouse body weights and abnormal behaviors were followed for two weeks after administration, as described in more detail in SI.

2.6. Cells used for in vitro and in vivo antitumor efficacy studies

Cells used for *in vitro* and *in vivo* antitumor efficacy studies were U87-MG Luc human GBM cells transduced with a Neo-luciferase gene, U87-Luc. After thawing, U87-Luc adherent cells were cultivated at 37 °C in the presence of 5% CO_2 in Dulbecco's Modified Eagle Medium (DMEM) containing 10% fetal bovine serum (FBS). Once the cells reached confluence, the culture dishes were rinsed with Hank's Balanced Salt Solution (HBSS). Cells were then detached by trypsinization for 5 minutes at 37 °C in the presence of 5% CO_2. The action of trypsin was stopped by addition of the medium containing FBS. The cellular concentration was determined using a Malassez cell, and the cells were then used for *in vitro* and *in vivo* antitumor efficacy studies.

2.7. Apoptosis and necrosis induced by M-PLL and IONP brought into contact with U87-Luc cells in the presence (or not) of an alternating magnetic field

The *in vitro* antitumor efficacy of M-PLL and IONP towards U87-Luc tumor cells was determined by bringing into contact 1 mg/mL in iron of these nanoparticles with U87-Luc cells for 30 minutes and by exposing (or not) these assemblies to an AMF of 202 kHz and 27 mT for 30 minutes to produce a temperature increase of 4-7 °C (Figure S-8), which was measured with an infrared camera. Following treatments, cells were incubated for 24 hours at 37 °C in the presence of 5% CO_2. They were then harvested, mixed with Annexin V (apoptosis detection) and Propidium iodide (necrosis detection), and introduced in the cytometer where luminescence intensities of Annexin V and Propidium iodide were detected following excitation at 488 nm. This enabled the determination of the percentage of apoptosis and necrosis among treated U87-Luc cells, as detailed in the SI.

2.8. In vivo antitumor efficacy studies of M-PLL and IONP

2.8.1. Ethical considerations

In vivo experiments were carried out following the ethical guidelines of the Institutional Animal Care and Use Committee ("Ethic committee Charles Darwin N° 5"). In particular, mice were fed and watered according to these guidelines and were euthanized by cervical dislocation when their weight had decreased by more than 20% relative to their initial weight before tumor cell implantation or when signs of pain, unusual posture or prostration were observed.

2.8.2. Animals

Pathogen-free 5-week-old athymic female nude mice of mean weight 18 g, purchased from Charles River, were used for *in vivo* experiments.

2.8.3. Models of Intracranial U87-Luc cells in mice

Before being mounted in a stereotactic frame, mice were anesthetized with a mixture of Ketamine (100 mg/kg) and Xylazine (8 mg/kg). To achieve the surgical procedure leading to cell implantation, a craniotomy was carried out and 2 µl of a suspension containing 2.10^5 U87-Luc cells was

187 injected into the right caudate nucleus putamen (relative to bregma in mm: 0.2.2) designated as (0.2.2)
188 mm.

189 *2.8.4. In Vivo treatment groups*

190 Six groups of mice with induced tumors, as described in section 2.8.3, were subjected to
191 different treatment protocols (Table S-4). Each group contained 9 mice. At day 0 (D0), a cell suspension
192 containing 10^5 U87-Luc cells per microliter was first injected into the brains of mice. The tumor grew
193 for 5 days between D0 and D5. At D5, 6 different groups of mice received at the tumor cell implantation
194 coordinates, (0.2.2) mm, 2 µl of different solutions or suspensions containing either 5 % of glucose
195 (groups I and II), 500 µg in iron of M-PLL (groups V and VI) or 500 µg in iron of IONP (groups III and
196 IV). Groups I, III, and V were not treated further after D5, whereas groups II, IV, and VI were exposed
197 to 15 magnetic sessions (MS) at D5, D6, D7, D12, D13, D14, D19, D20, D21, D26, D27, D28, D33,
198 D34, D35 for group II, to 23 MS at D5, D6, D7, D12, D13, D14, D19, D20, D21, D26, D27, D28, D33,
199 D34, D35, D40, D41, D42, D47, D48, D49, D54, D55 for group IV, to 27 MS at D5, D6, D7, D12, D13,
200 D14, D19, D20, D21, D26, D27, D28, D33, D34, D35, D40, D41, D42, D47, D48, D49, D54, D55,
201 D56, D61, D62, D63 for group VI. Each magnetic session included the application of an AMF with a
202 frequency of 202 kHz and strength of 27 mT for 30 minutes. A second administration of 200 µg in iron
203 of M-PLL or IONP was carried out at D47 due to tumor regrowth in 8 mice from group IV (M28, M29,
204 M30, M31, M32, M33, M34, M36) and in 4 mice from group VI (M47, M52, M53, M54).

205 *2.8.5. Estimate of tumor volume from tumor bioluminescence intensity of living GBM cells*

206 Tumor bioluminescence intensity (BLI) measurements were carried out one day before each
207 magnetic session to follow tumor size variations using an IVIS Spectrum System (in vivo imaging
208 system, PerkinElmer, Inc., Walther, MA). Ten minutes before BLI measurement, a suspension of
209 luciferin was administered intraperitoneally to the mice. When luciferin reacted with the ATP of living

GBM cells, it produced oxyluciferin, which is luminescent. BLI, which is therefore proportional to the number of live GBM cells, can be used to detect the presence of live GBM cells.

Furthermore, a relation between BLI and tumor volume was established (Figure S-7) by measuring at D7, D14, D21, D28 and D35 both BLI in living mice and in tumor volumes using histological analysis of tumors collected from mice euthanized on the same days. A linear relation was found between the logarithm of the tumor bioluminescence intensity, log(BLI), and the logarithm of the tumor volume expressed in mm^3, log(volume(mm^3)), shown in Figure S-7. A linear coefficient of 1.4 was deduced from fitting the plot of Figure S-7, a value that agrees with previously reported ones [36, 37, 38]. The average tumor volume (ATV) in the various groups of mice was measured by histological analysis at D5 as ~1.5 mm^3.

2.8.6. Intratumor temperature measurements during treatment.

Temperature distribution in the tumor was measured as a function of time during the various treatments using an infrared camera (EasIRTM-2, Optophase) placed 20 cm above the coil. Maximum temperatures within the tumor region were then deduced from each infrared image, representing spatial temperature distribution in the tumor region. They were plotted as a function of time for the various treatments. Due to the shallowness of the tumor, the temperature measured with a thermocouple microprobe (IT-18, Physitemp, Clifton, USA) in the region of nanoparticle injection was the same as that of the maximum temperature deduced from the infrared image. The distribution of heat in the tumor therefore appeared similar to that at the brain surface, which is measured with an infrared camera.

2.8.7. Statistical analysis

Mouse survival rates were plotted using the Kaplan-Meier model method [40, 41]. Statistical significance of survival rates in the different groups was evaluated using the log rank test. The parameters were expressed as the mean ± SD and as p-values estimated relative to group I [15].

2.9. Estimate of nanoparticle SAR in vitro and in vivo

The specific absorption rate, SAR, of the various nanoparticles, expressed in Watts per gram of nanoparticle in iron, was estimated using the formula: $SAR=C_v(\Delta T/\delta t)/X_{Fe}$, where C_v = 4.2 J/gK is the specific heat capacity of water, $\Delta T/\delta t$ is the initial slope of the temperature variation with time, estimated in °C/sec, and X_{Fe} is iron concentration in g/mL provided by the nanoparticles. The protocols used to heat the various nanoparticles *in vitro* and *in vivo* are described in sections 2.7 and 2.8.4, respectively. The values of $\Delta T/\delta t$ were deduced from the initial slopes of the plots of Figure S-5 for *in vitro* heating and of Figures 5(c) and 6(c) for *in vivo* heating. The values of the specific absorption rates measured *in vitro* and *in vivo* are provided in Table S-2.

2.10. Histological analysis

Histological studies were carried out on brains extracted from euthanized mice, which were fixed with a 4% solution of paraformaldehyde, cut into transverse slices of 2 mm thickness and included in paraffin. Sections of paraffin blocks with a 4 µm thickness were deposited on glass slides and stained with hematoxylin-eosin (H&E) to distinguish between healthy and tumor areas. Histological analysis was carried out on mice that received M-PLL at D5 and were euthanized 6 hours following M-PLL injection (Figures S-9(a) and S-9(c)) or 72 hours (Figures S-9(b) and S-9(d)); or 6 hours following M-PLL injection and one MS (Figures 8(a) and 8(c)); or 72 hours following M-PLL injection and three MS (Figures 8(b) and 8(d)). The same histological analysis was done for IONP nanoparticles on mice euthanized at (i) 6 or 72 hours after IONP administration (Figures S-10(a) and S-10(b)); (ii) 6 hours following IONP injection and one MS (Figure S-10(c)); or (iii) 72 hours following IONP injection and three MS (Figure S-10(d)).

3. RESULTS AND DISCUSSION

To fabricate M-PLL, we first grew gram-negative MSR-1 magnetotactic bacteria. The TEM image of Figure 1(a) shows a typical magnetotactic bacterium that contains a long chain of nanoparticles called magnetosomes. The latter are used by magnetotactic bacteria as a magnetic compass to navigate

in the direction of earth's magnetic field. Their sizes, assembly, and magnetic properties have been optimized over time by these bacteria to enable an alignment of the magnetosome magnetic moment parallel to earth's magnetic field [42]. This leads to better magnetic properties for magnetosomes than for most chemically synthesized nanoparticles and makes magnetosomes especially appealing for medical applications [43]. However, in the absence of specific processing, the magnetosome mineral core is surrounded by potentially toxic and pyrogenic organic material, which is also difficult to characterize.

3.1. Physical, chemical, and toxicity properties of uncoated magnetosome minerals (M-Uncoated)

In this study, the organic material was mostly removed by isolating magnetosomes from magnetotactic bacteria and treating the extracted magnetosomes with several detergents (NaOH, phenol, chloroform, SDS) combined with heat and sonication (see SI). This led to uncoated magnetosome minerals, M-uncoated. Following these processes, the presence of a low quantity of organic material at the surface of the magnetosome mineral core was highlighted on the one hand by CHNS analysis (Figure 2(c)), which revealed a low percentage of Carbon (2.4%) and Nitrogen (0.2%) in M-Uncoated, and on the other hand by FT-IR spectra that displayed two dominant bands at 609 and 673 cm^{-1}, attributed to iron oxide, and three weaker bands at 1041 cm^{-1}, 2933 cm^{-1}, and 3295 cm^{-1}, which most likely arise from NH, CH, PO and OH bonds in the organic material surrounding the magnetosome mineral core that remained after treatments (Figure 2(a)). In M-Uncoated, the composition of the magnetosome mineral core was determined to be maghemite from saturating isothermal remnant magnetization (SIRM) measurements, which did not show the Verwey transition (Figure S-2(b)). Due to their relatively large size of 45 nm (Figure 1(e)), M-Uncoated produced magnetic hysteretic behavior at room temperature with ratios between remnant and saturating magnetizations, M_r/M_s, saturating magnetization, M_s, and coercivity, H_c, of 0.24, 64 Am^2/kg, and 10 mT, respectively (Figure S-2(a), Table S-1). Furthermore, suspensions of M-Uncoated contained a low endotoxin level of 10-100 $EU.mL^{-1}.mg^{-1}$.

Concentrations of 15 to 1000 µg/mL of M-Uncoated brought into contact with 3T3 cells did not induce any cell inhibition, indicating that M-Uncoated were non-cytotoxic (Figure S-4(a) and section 2.5). Despite these properties, M-Uncoated tend to aggregate, as revealed by the TEM image of M-Uncoated presented in Figure S-1(a) and by the rapid decrease in optical absorption by more than 80% in 20 minutes of a suspension of M-Uncoated, measured after nanoparticle homogenization (Figure S-1(b)). For medical applications, aggregation should be avoided since it can prevent thorough administration and can lead to embolism in the organism.

3.2. Physical, chemical, and biocompatibility properties of magnetosome minerals coated with poly-L-lysine (M-PLL)

To prevent their aggregation, improve their heating properties and enable their administration, M-uncoated were coated with a polycationic polymer, poly-L-lysine, yielding M-PLL. In M-PLL, the presence of a poly-L-lysine coating was first revealed by the TEM image of M-PLL (Figures 1(b) and 1(c)), which shows seven magnetosomes with a mineral core coated with a 4- to 17-nm-thick layer of organic material. Also highlighted by the FT-IR spectrum of M-PLL presented in Figure 2(a) are bands at 1546 cm^{-1} and 1656 cm^{-1}, which are not in the FT-IR spectrum of M-uncoated (Figure 2(a)) and are attributed to the NH and C=O bonds of the amide groups of poly-L-lysine. Third, CHNS analysis indicated a higher percentage of Carbon and Nitrogen in M-PLL (5 and 1%, respectively) than in M-uncoated (Figure 2(c)). Fourth, the zeta potential of a M-PLL suspension was positive over a wider range of pH for M-PLL ($2 < pH < 8$) than for M-uncoated ($pH = 2$), as shown in Figure 2(b) and Table S-1, suggesting the presence of a positively charged material such as poly-L-lysine at the surface of the magnetosome mineral core in M-PLL. M-PLL also tend to form chains (Figure 1(b)), an organization that prevents aggregation and leads to well-dispersed nanoparticles, as shown in the TEM images of Figures 1(b) and 1(c). Furthermore, as for M-Uncoated, M-PLL produced magnetic hysteretic behavior at room temperature with M_r/M_s ~0.19 (Figure S-2(a)), M_s ~ 72 Am^2/kg, and H_c ~ 5 mT (Table S-1). Magnetic hysteretic parameters of M-PLL differ significantly from those of M-Uncoated, possibly due to different types of nanoparticle interactions.

As for M-uncoated, M-PLL suspensions contained a low endotoxin concentration of 78 EU $mL^{-1}mg^{-1}$, as deduced by the LAL assay, leading to an absence of pyrogenicity in the rabbit test, *i.e.*, a rabbit temperature increase of 0.38 °C following injection of 5 mg of M-PLL in its ear, which is less than the limit of 0.5 °C necessary to pass the test (see SI). Since the percentage of 3T3 cell inhibition varied between 16 µg/mL and 1 mg/mL in iron and was less than 30% when these cells were brought into contact with M-PLL at concentrations, M-PLL also appeared relatively non-cytotoxic (Figure S-4(a) and section 2.5). M-PLL also seemed slightly more cytotoxic than M-Uncoated, which may be due to M-PLL internalizing cytotoxic poly-L-lysine, as expected for a transfecting agent and as observed for U87 cells (Fig. 3(e)). Direct injection in the brain at (0.2.2) mm of 0.5 mg iron of M-PLL, which is equivalent to the initial administered therapeutic dose, did not induce weight loss during the two weeks following injection, indicating that such a dose was safe (Figure S-6(c)). For this same quantity and higher doses of 1 to 4 mg of M-PLL, acute systemic toxicity was not observed (Figure S-6(a)), indicating that if M-PLL was going to leak in the vascularization system after leaving the brain, this night not induce toxicity. Furthermore, the optical absorption of a M-PLL suspension decreased by less than 20% in 20 minutes (Figure S-1(b)) and M-PLL suspensions remained stable for 4 hours following their preparation (Figure S-11). M-PLL therefore appeared to be sufficiently stable and nontoxic to be safely administered in mice.

3.3. Physical, chemical, and biocompatibility properties of IONP

Compared with M-PLL, chemically synthesized iron oxide nanoparticles (IONP) were characterized by more irregular shapes and smaller sizes of 17 to 20 nm, as shown in the TEM image of Figure 1(d). The surface of IONP also differed from that of M-PLL, as revealed first by CHNS measurements that indicated percentages of carbon and nitrogen in IONP of 9 and 0%, respectively, and second, by the FT-IR spectrum of IONP (Figure 2(a)) that displays three dominant bands attributed to iron oxide at 610 and 673 cm^{-1} and starch polymer at 1025 cm^{-1} and 1150 cm^{-1}. Furthermore, over a wide range of tested pH values ($2<pH<8$), the zeta potential of the IONP suspension appeared to be less positive than for M-PLL

(Figure 2(b)). IONP displayed lower values of M_s ~ 47 Am^2/kg and of M_r/M_s ~ 0.15 but a higher value of H_c ~ 11 mT compared with M-PLL.

Due to their chemical synthesis, IONP suspensions contained a low endotoxin concentration of 50 EU $mL^{-1}mg^{-1}$. Under similar conditions of toxicity assessment as for M-PLL, IONP appeared to be non-cytotoxic towards 3T3 cells (Figure S-4(a)) and not to lead to any toxicity following administration in the brain or in the tail of mice (Figures S-6(d) and S-6(b)). In addition to being nontoxic, the IONP suspension remained stable during 20 minutes of absorption measurement, which suggests that they could safely be administered to mice (Figure S1(b)).

3.4. In vitro heating and cytotoxic properties of M-PLL and IONP

Next, nanoparticle heating and toxicity properties in the presence of U87-Luc cells under application (or not) of an AMF were examined. To be able to increase the temperature of an assembly of tumor cells and nanoparticles by a quantity similar to that reached in a hyperthermia treatment, *i.e.*, by ~ 8 °C and ~ 5 °C for M-PLL and IONP, respectively (Figure S-5), we brought into contact 1 mg/mL of IONP and M-PLL with U87-Luc cells and we applied an AMF of 27 mT and a frequency of 202 kHz for 30 minutes.

The percentage of cell death of these assemblies increased from 60% and 0.2% before AMF application to 90% and 8.1% after AMF application for M-PLL and IONP, respectively (Figures 3(a) to 3(d)). Overall, M-PLL appeared to be more cytotoxic than IONP both in the absence and presence of the AMF, a behavior that may be attributed to the M-PLL nanoparticle chain arrangement that could enhance nanoparticle interactions with cells, to PLL intrinsic cytotoxicity [44], or to M-PLL being more strongly internalized in U87-Luc cells than IONP (Figure 3(e)), possibly resulting in enhanced PLL intracellular interactions. Part of this behavior may also be due to the higher specific absorption rate (SAR) of M-PLL (SAR = 52 W/g_{Fe}) than IONP (SAR = 39 W/g_{Fe}), as deduced from the initial slopes of the *in vitro* temperature variations with times of both types of nanoparticles following AMF application (Figure S-5 and Table S-2). Furthermore, cell death in the presence of nanoparticles mainly appeared to be apoptotic in the presence (or not) of the AMF. Interestingly, the percentage of cell death due to apoptosis among

all dead cells increased from 43% and 50% before AMF application (Figures 3(a) and 3(c)) to 70% and 99% after AMF application (Figures 3(b) and 3(d)) for M-PLL and IONP, respectively, suggesting that a moderate temperature increase of 5-8 °C (Figure S-5) strongly favors apoptosis versus necrosis [45].

3.5. Antitumor efficacy in mice bearing intracranial U87-Luc tumors treated by intratumor administration of M-PLL and IONP followed by magnetic sessions

To compare the antitumor efficacy of M-PLL with that of IONP in the treatment of GBM using magnetic hyperthermia, mice bearing intracranial U87-Luc tumors were treated following the protocol described in section 2.9. Five days following U87-Luc cell implantation at brain coordinate (0.2.2) mm, intracranial U87-Luc tumors had reached an average size of ~1.5 mm^3. Mice were then separated into the 6 aforementioned different groups and were treated as follows. Control groups I and II received at (0.2.2) mm an intra-tumor administration of glucose without AMF application (group I) or followed by 15 magnetic sessions (group II). Other mice received 500 µg in iron of M-PLL or IONP at (0.2.2) mm without any further treatment (groups III and V), or one or two administrations of 500 or 700 µg of these nanoparticles with 23 to 27 magnetic sessions (groups IV and VI). Each magnetic session consisted in the application of an AMF of 27 mT and 202 kHz for 30 minutes.

Nanoparticle treatments with/without AMF application appeared to be safe because signs of toxicity (body weight loss, prostration, pain) were not observed in mice 2 weeks following administration. To follow tumor size evolution, the luminescence intensity of U87-Luc tumor cells, which was shown to be proportional to the tumor volume (Figure S-7), was measured using an in vivo imaging system (IVIS) spectrum every 7 days after tumor cell implantation.

For the control groups I (G5 injection only) and II (G5 injection with MS), average tumor volumes (ATV) increased exponentially from 1.5 mm^3 at D0 to 180-200 mm^3 at D45 (Figure 4(a) and 4(b)). Signs of antitumor activity were not observed, and these mice had to be rapidly euthanized at D40-D54. Whereas mice belonging to group III (IONP administration) displayed a similar behavior to those of the control groups I and II, those of group V (M-PLL administration) had delayed tumor growth, leading to

longer survival by 100 days compared with control groups I and II (Figures 4(e) and 7) and indicating clear but only partial anti-tumor activity. This behavior could be attributed to M-PLL cytotoxicity and led to a median survival day (MSD) of 111, $p<0.0001$*, which was larger than that of 46, $0.338<p<0.662$ measured for groups II and III.

In group VI, the administration of M-PLL followed by 27 MS strongly enhanced antitumor efficacy, leading to an ATV, initially at 1.5 mm^3 at D4, which either continuously decreased in five mice (M46, M48, M49, M50 and M51) or decreased, increased, and decreased again following a second nanoparticle administration at D47 in four other mice (M47, M52, M53, and M54), as shown in Figure 4(f). These two types of behaviors are highlighted in Figures 5(a) and 5(b), which show variations in tumor volumes with corresponding BLI of brain tumors as a function of time for mice M54 (Figure 5(a)) and M51 (Figure 5(b)). They led to full tumor disappearance at D30 to D68, respectively, and to 100% of mice being alive at D350 (MSD=350, $p<0.0001$*). The efficacy of the treatment could be attributed to magnetosomes remaining in the brain for a long period of time. M-PLL were indeed observed 72 hours after 3 MS (Figure 8(b)) and 250 days after treatment (Figure 9(b)), possibly enabling a coupling between the applied magnetic field and the magnetosomes during this time period, hence yielding persistent antitumor activity. Mice were euthanized at D350 for histological analysis of their brains, revealing the absence of tumor cells, lesions, and edema without (Figure 9(a)) or with (Figure 9(b)) nanoparticle remains. Overall, the treatment was efficient and safe. Healthy tissues surrounding the tumor appeared not to be damaged by hyperthermia (absence of edema and necrosis/apoptosis), as observed 72 hours after 3 MS in Figure 8(b) or 250 days after treatment in Figures 9(a) and 9(b).

Compared with mice belonging to group VI, those of group IV (IONP administration and magnetic sessions) were prone to less significant antitumor efficacy. The AVT either increased from 1.5 mm^3 at D0 to 150 mm^3 at D50 in 7 mice (M28, M30, M31, M32, M33, M34 and M36) with an observed tumor growth delay compared with mice belonging to groups I, II and III or disappeared fully at D55 without tumor regrowth in 2 mice (M29 and M35). These two types of behaviors are exemplified in Figures 6(a)

for M35 and 6(b) for M29, which show that tumor volume either continuously decreased (Figure 6(a)) or increased less rapidly than in groups I to III (Figure 6(b)), yielding an MSD of 57, $p<0.0001$*.

3.6. More intense and persistent tumor heating reached with M-PLL than with IONP

Full tumor disappearance was associated with heat produced by nanoparticles in the presence of U87-Luc tumor cells, since in the absence of heating, the tumors continued to grow following nanoparticle administration (M-PLL or IONP administration without MS, Figures 4(c) and 4(e)). We therefore examined *in vivo* nanoparticle heating properties of mice belonging to groups IV (IONP + MS) and VI (M-PLL + MS). During the first MS, where both types of nanoparticles produced heat, the temperature increase measured over the whole MS, ΔT, and the SAR deduced from the initial slopes of the plots of Figures 5(c) and 6(c) for M-PLL and IONP, respectively, were higher for M-PLL (ΔT_{30min} = 17.5 °C and SAR = 1.3 W/g_{Fe}) than for IONP (ΔT_{30min} = 8.5 °C and SAR = 0.2 W/g_{Fe}), a behavior that corroborates the heating properties observed *in vitro* (Figure S5). Furthermore, tumors could be heated during a larger number of MS with M-PLL than with IONP, *i.e.*, during 16 and 1 MS following the first nanoparticle administration and during 9 and 1 MS following the second nanoparticle administration for M-PLL and IONP, respectively (Figures 5(c), 5(d), 6(c) and 6(d)). We also measured that the ratio between the surface representing the distribution in temperatures, which are more than 1 °C above mouse physiological temperature and the tumor surface, is ~ 2% during the 20 first MS, then increases from 2 to 6% between the 20^{th} and 25^{th} MS for M-PLL, whereas it decreases from 1% to 0% between the first and fifth MS for IONP (Figure S-8). M-PLL could therefore be heated for a longer period of time than IONP. The higher heating power and more persistent tumor heating observed for M-PLL than IONP do not, however, seem sufficient to fully explain the enhanced M-PLL antitumor activity. Indeed, the percentages of areas within heated tumors reached with both types of nanoparticles are small, *i.e.*, below 6% (Figure S-8), which may be attributed to the partial tumor occupation by nanoparticles, as deduced from histological analysis (Figures 8(a) and 8(b) and Figures S-10(c) and S-10(d)). We concluded from this observation that tumor destruction was not only directly induced by heat.

3.7. Possible indirect mechanisms leading to enhanced anti-tumor efficacy with M-PLL than with IONP

We therefore studied the possible mechanisms involved in tumor destruction outside the heated region. As observed *in vitro*, M-PLL led to enhanced apoptotic cell death in the presence of AMF; *i.e.*, 63% (Figure 3(b)) compared with 8% for IONP (Figure 3(d)). *In vivo* U87-Luc cell death may also mainly be due to apoptosis since temperature increases, which have been suggested to be responsible for the cell death mechanism [46], were relatively similar *in vitro* and *in vivo* during the first MS at 8-17.5 °C for M-PLL (Figures 5(c) and S-5) and 5-8.5 °C for IONP (Figures 6(c) and S-5). Apoptosis may induce cellular death at a certain distance from the region which is heated or contains nanoparticles through a thermal bystander effect, possibly leading to antitumor activity occurring within the whole tumor volume [47,48].

Heat may also result in stronger micro-vascular damage for M-PLL than IONP, since M-PLL were observed in the ventricles near the blood vessel for a longer time (6 and 72 hours, Figures S-9(a) to S-9(d)) than IONP (6 and 72 hours, Figures S-10(c) and S-10(d). This possibly led to the enhanced destruction of the blood vessels supplying the tumor with oxygen [49] and, therefore, to stronger tumor asphyxia with M-PLL than with IONP.

The immune system, although only partially activated in nude mice, may also possibly be involved in antitumor activity [50]. Indeed, polynuclear neutrophils (PNN), which were observed 6 hours following M-PLL administration (Figures 8(a), 8(c), S-9(a) and S-9(c)) may possibly target M-PLL and destroy tumor cells surrounding them. Interestingly, they did not seem to be recruited by endotoxins because the percentage of endotoxins released by M-PLL and IONP following MS was similar and low (Figure S-3), but this may have occurred due to poly-L-lysine or inflammation [51].

Finally, poly-L-lysine cytotoxicity, observed in the absence of MS application (Figure S-4(b)), may be enhanced by MS due to the production of localized heat or to the detachment of poly-L-lysine from the magnetosome mineral core, as described elsewhere with pyrogenic chains of magnetosomes. Poly-L-

lysine diffusion away from M-PLL may induce tumor cell destruction outside the region that was heated or contained nanoparticles.

4. CONCLUSION

We have presented a method for producing magnetosomes synthesized by magnetotactic bacteria in which magnetosomes are extracted from these bacteria, purified to remove most organic material and endotoxins, and then coated with poly-L-lysine to form a stable suspension of M-PLL. We have shown that M-PLL are pyrogen-free, non-toxic and that they yield *in vitro* and *in vivo* a larger amount of heat than IONP, thus enabling enhanced tumor cell destruction.

Thus, when 500 to 700 μg of M-PLL in iron was administered to intracranial U-87 luc tumors of 1.5 mm^3 and the tumors were exposed to an alternating magnetic field of 27 mT and 202 kHz, applied 27 times for 30 minutes, all of the mice were alive and apparently cured 350 days following injection.

The observed antitumor activity did not appear to be solely due to the direct destruction of the tumor cells by temperature increase since the latter was only observed in a portion of the tumor. In addition, we observed full tumor destruction for M-PLL occupying part of the tumor, which is desired for GBMs that are infiltrating and can therefore hardly be fully covered by nanoparticles. We have identified four other possible mechanisms of tumor destruction in non-heated regions. These are apoptotic tumor cell death, destruction of blood vessels irrigating the tumor, recruitment of polynuclear neutrophils, and a cytotoxic effect of poly-L-lysine.

Finally, compared with previous preclinical studies showing increased survival of 15-44 days in rats bearing RG-2 or T-9 glioma tumors and treated by magnetic hyperthermia at 43-47 °C [15, 19] and with IONP that resulted in 20% of mice with full tumor disappearance, M-PLL led to enhanced antitumor efficacy with full U87-Luc tumor disappearance in 100% of treated mice.

ACKNOWLEDGMENTS

ACCEPTED MANUSCRIPT

We would like to thank the Eurostars program (Nanoneck-2, E9309), subvention AIR from the region of Paris (A1401025Q), the ANRT, the ANR (Méfisto project), the French Research Tax Credit Program, Paris Biotech Santé, BPI, the University Paris 6, the University Paris XI. Research presented in this manuscript was directed by Edouard Alphandéry. Jean-Yves Delattre, Ahmed Idbaih, and Charlotte Schmitt commented on the relevance of the preclinical protocol to verify that it is clinically applicable, since this group may possibly be in charge of the clinical trials using this treatment. We thank Clovis Adam and the platform 'Histim' of the Cochin Institute for their help concerning histological experiments, JM Guigner for TEM and S. Morosan, O. Bregerie, B. Kane and A. Jacquet for their help concerning in vivo imaging and keeping the animals healthy. We also thank Laure Cordier for their help concerning ICP measurement. This work was supported by the IPGP multidisciplinary program PARI and by Région Ile-de-France SESAME Grant No. 12015908.

Supplementary Information (SI)

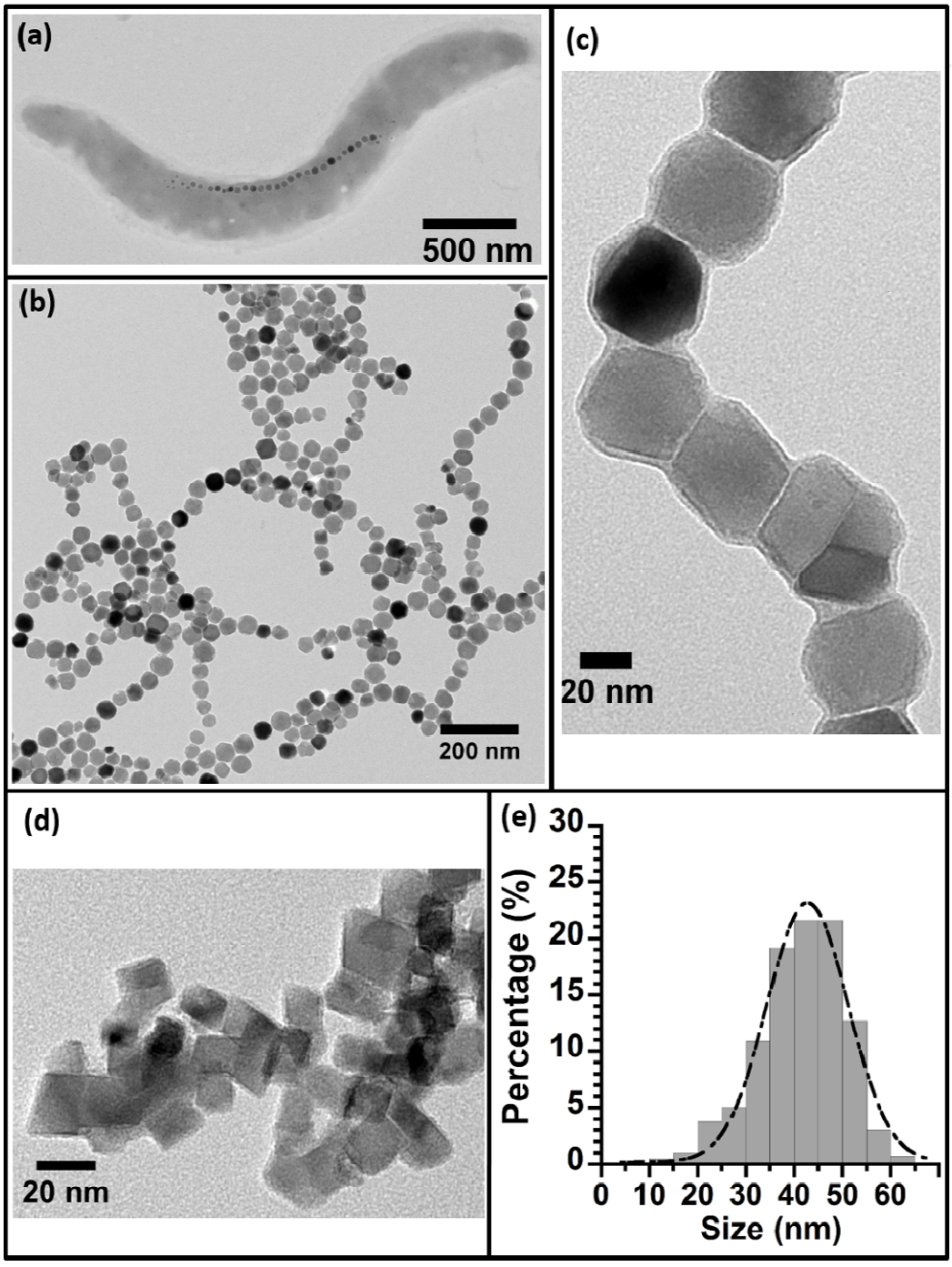
Fabrication of M-Uncoated, M-PLL, and IONP, the methods used for nanoparticle characterization, cytotoxicity assessment, and *in vivo* efficacy and toxicity evaluation, are described.

ACCEPTED MANUSCRIPT

498 **FIGURES**

499

500



501

502 **Figure 1** Transmission electron microscopy images of a MSR-1 *Gryphiswaldense* magnetotactic

503 bacterium (a) of magnetosome minerals coated with poly-L-lysine organized in chains, M-PLL, (b), (c),

504 and of IONP (d). (e) Histogram representing the size distribution of uncoated magnetosome minerals,
505 M-Uncoated, where measurements were carried out on 300 magnetosomes.

506

ACCEPTED MANUSCRIPT

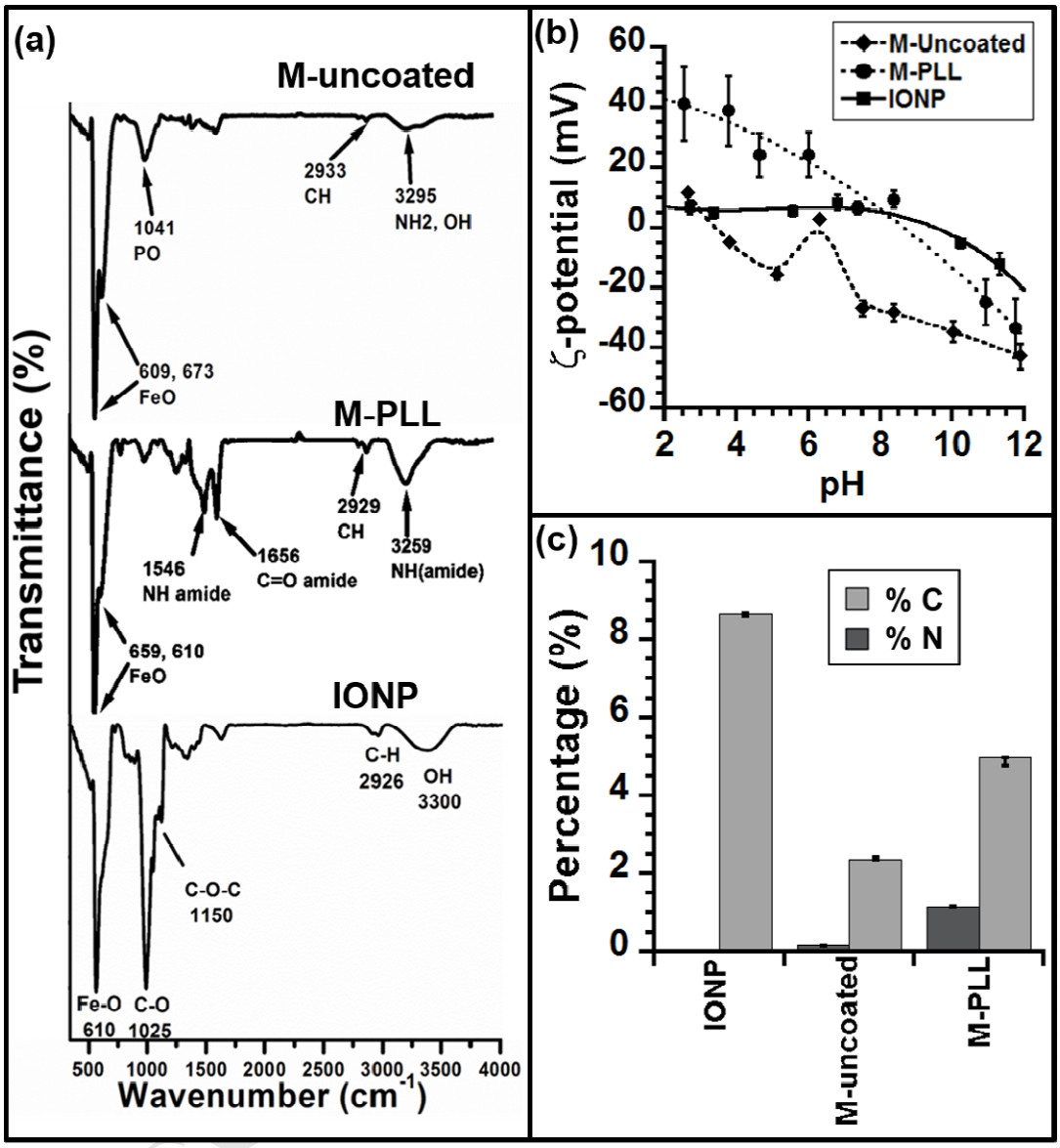


Figure 2 (a), FTIR spectra of uncoated magnetosome minerals, M-Uncoated, magnetosome minerals coated with poly-L-lysine, M-PLL, and iron oxide nanoparticles, IONP. (b), Zeta potential variations as a function as pH of suspensions of M-Uncoated, M-PLL, and IONP. (c), Percentages of carbon and nitrogen, measured with a CHNS analyzer, in M-Uncoated, M-PLL, and IONP.

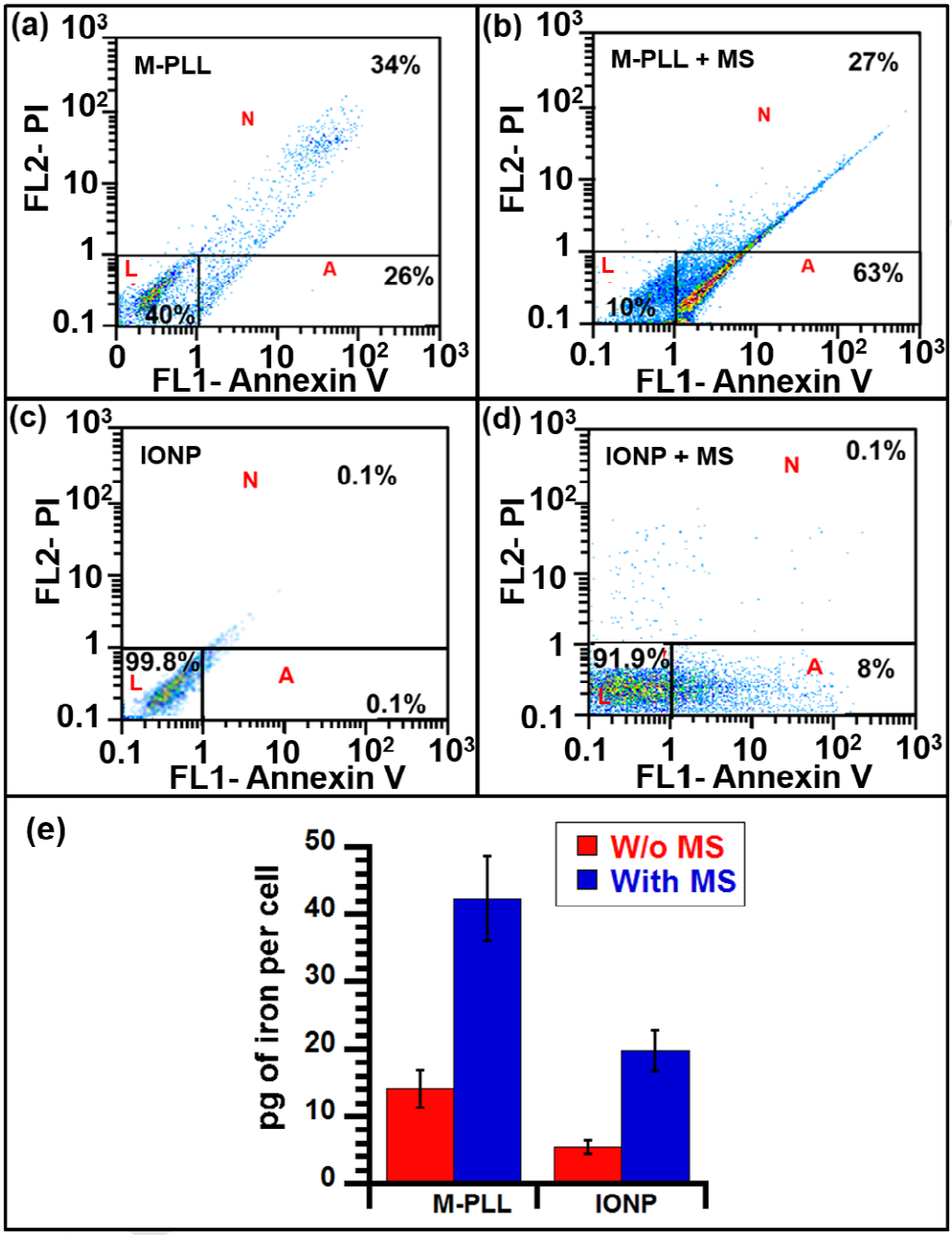


Figure 3 Fluorescence intensity of propidium iodide (FL2-PI) as a function of the fluorescence intensity of annexin V (FL1-Annexin V) for (a) 1 mg of M-PLL brought into contact with U87-Luc cells without AMF application, M-PLL, (b) 1 mg of M-PLL brought into contact with U87-Luc cells followed by one MS, M-PLL + MS, (c) 1 mg of IONP brought into contact with U87-Luc cells without AMF application, IONP, (d) 1 mg of IONP brought into contact with U87-Luc cells followed by one MS, IONP + MS (d).

522 (e) Quantity of iron originating from M-PLL and IONP, which is internalized, measured in pg of iron per
523 cell when 1 mg of IONP or M-PLL was brought into contact with U87-Luc cells, followed (or not) by
524 one MS. Each MS consisted in the application of an AMF of 27 mT and 202 kHz applied during 30
525 minutes. In (a) to (d), L, A and N, designate surfaces areas where each point designates a live, apoptotic,
526 or necrotic cell, respectively.
527

ACCEPTED MANUSCRIPT

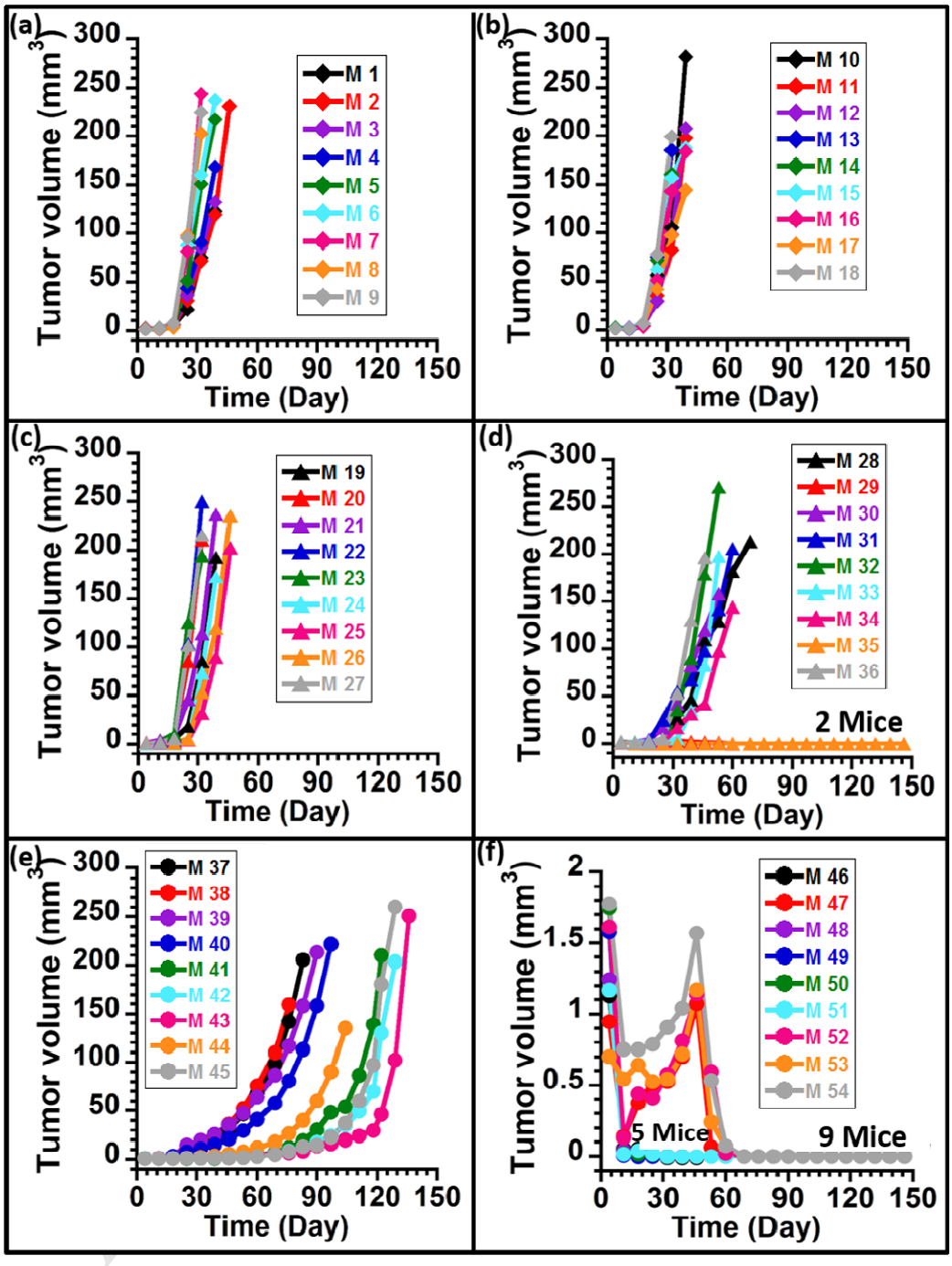
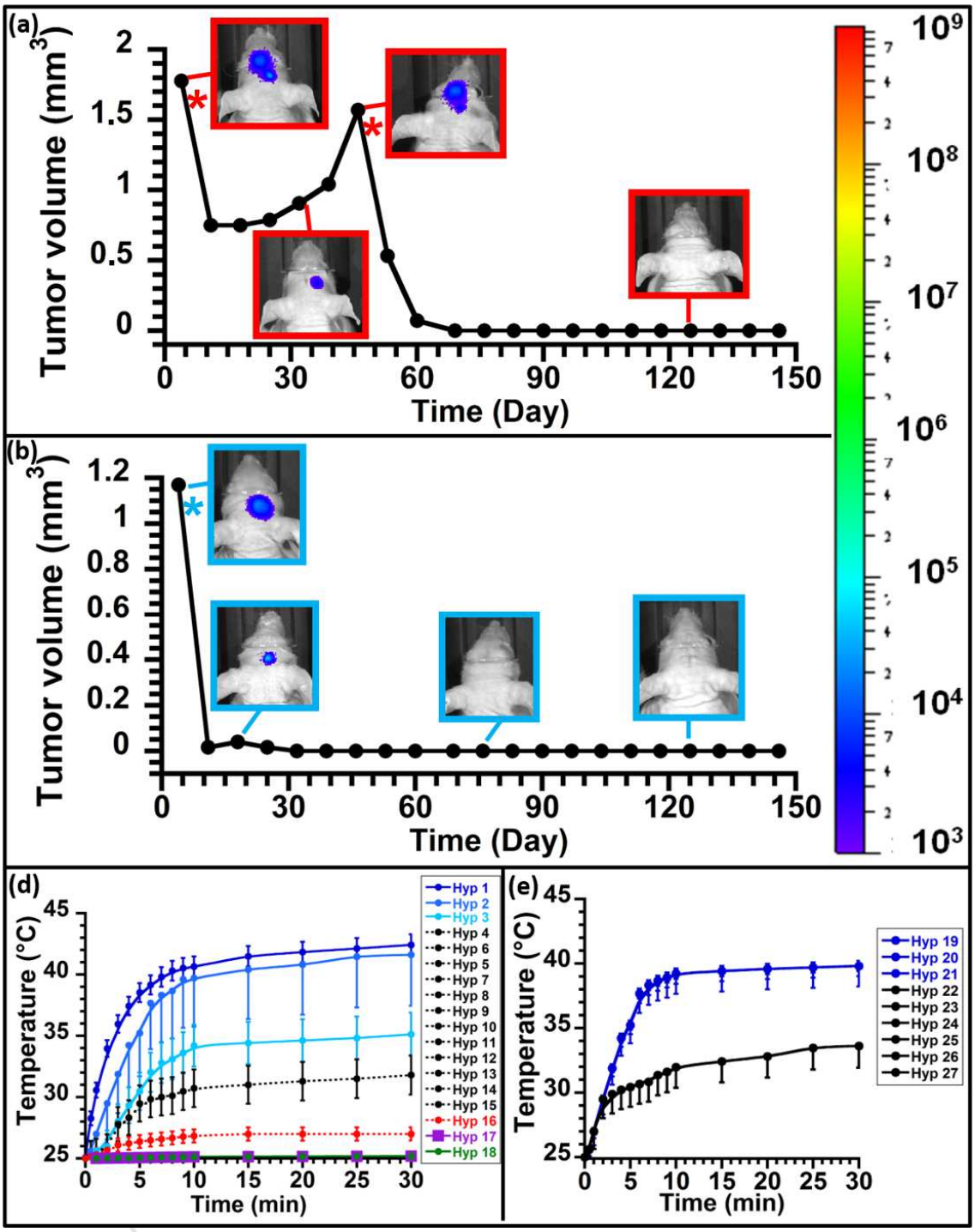


Figure 4 Variations in tumor volumes in mm^3 as a function of days following U87-Luc tumor cell implantation for mice belonging to groups I (glucose injection) (a) II (glucose injection with MS), (b) III (IONP administration), (c) IV (IONP administration with MS), (d) V (M-PLL administration), (e) VI (M-

PLL administration with MS) (f).

ACCEPTED MANUSCRIPT

537



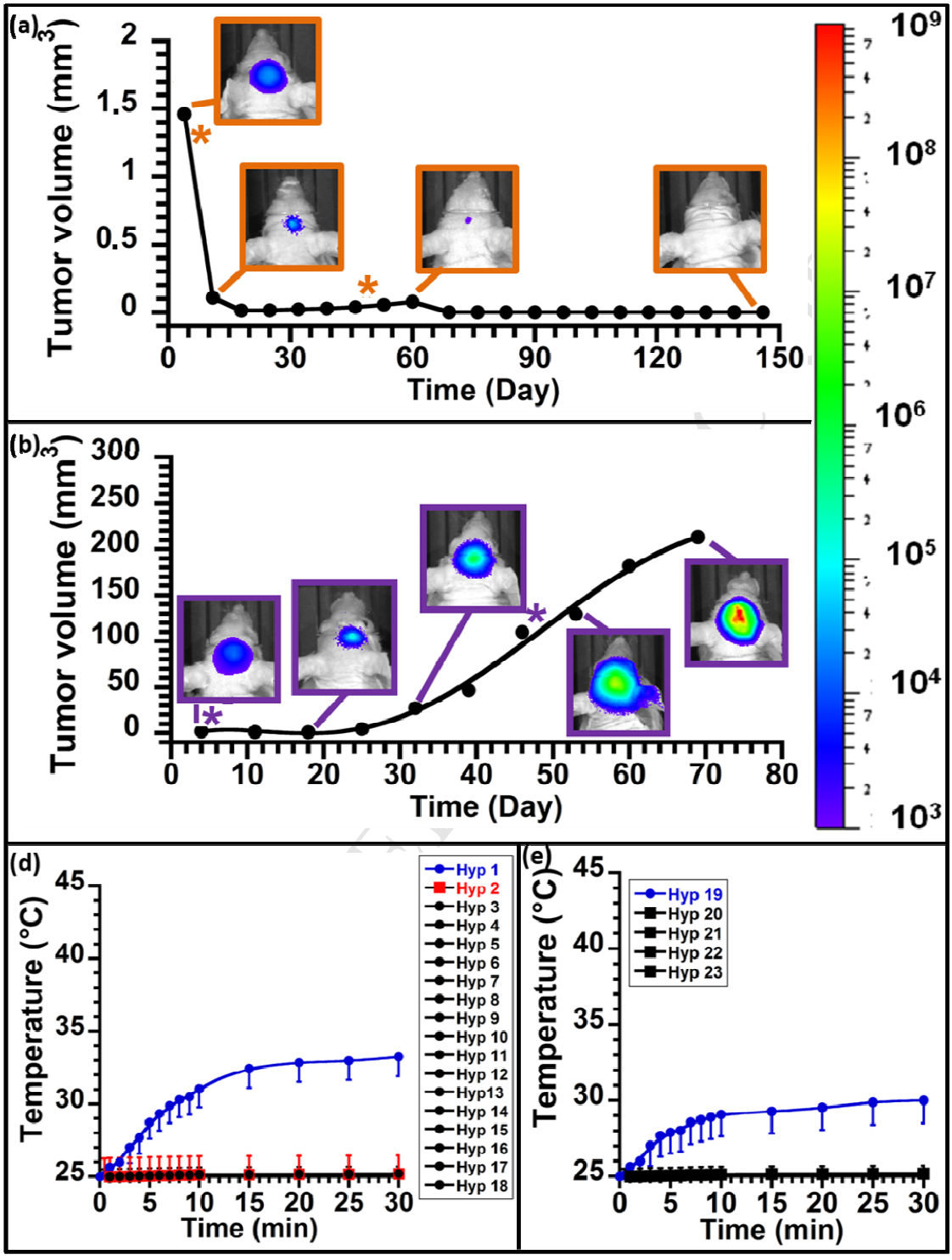
538

539 **Figure 5** Variation in tumor volumes in mm^3 as a function of days following U87-Luc tumor cell
540 administration for a mouse belonging to group VI with two M-PLL administrations (a) and for another
541 mouse of group VI with one M-PLL administration (b). Images of tumor BLI are shown at D4, D32,
542 D46, and D123 in (a), and at D4, D18, D74, and D123 in (b). In (a) and (b), the star designates the day at

543 which nanoparticles are administered in the tumor. Maximum temperatures deduced from the spatial
544 temperature distribution in the tumor as a function of time during each MS, following a first M-PLL
545 administration (MS1 to MS18) (c) or a second M-PLL administration (MS19 to MS27) (d). In (c) and
546 (d), maximum temperatures are average values deduced from measurements carried out on each mouse
547 belonging to group VI.
548

ACCEPTED MANUSCRIPT

549



550

551 **Figure 6** Variation in tumor volumes in mm^3 as a function of days following U87-Luc tumor cell
552 administration for a mouse belonging to group IV with full tumor disappearance (a), and for another
553 mouse of group IV with tumor growth delay (b). In (a) and (b), stars designate the day at which
554 nanoparticles were administered to the tumor. Images of tumor BLI are shown at D4, D11, D60, and

555 D144 in (a) and at D4, D18, D32, D53 and D67 in (b). Maximum temperatures deduced from the spatial
556 temperature distribution in the tumor as a function of time for the various MS following a first IONP
557 administration (MS1 to MS18) (c) or a second IONP administration (MS19 to MS23) (d). In (c) and (d),
558 maximum temperatures are average values deduced from measurements carried out on each mouse of
559 group VI.
560

ACCEPTED MANUSCRIPT

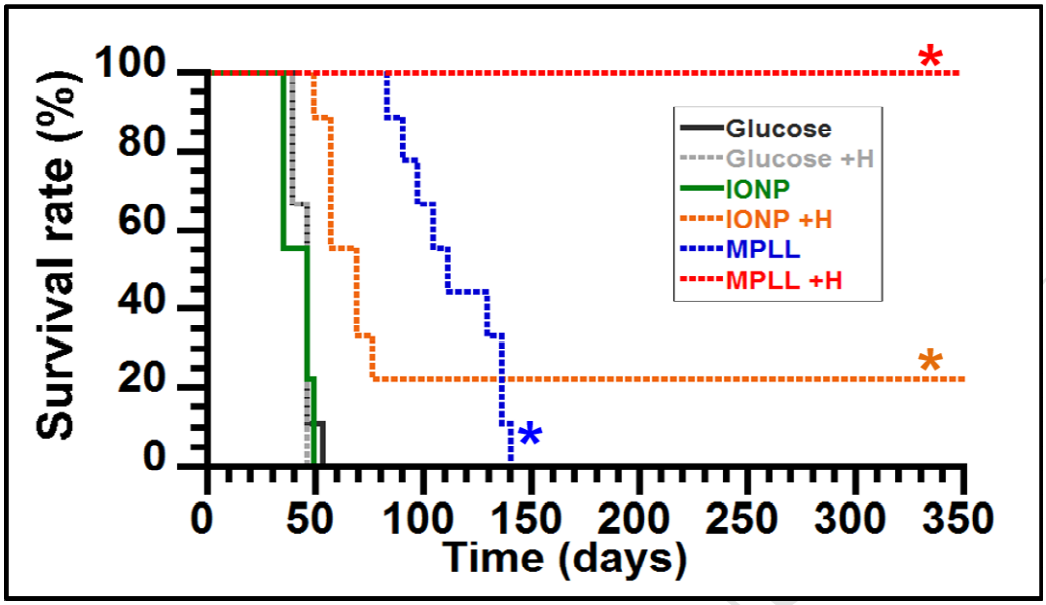


Figure 7 Percentage of survival as a function of days following nanoparticle administration for mice of groups I (glucose), II (glucose +H), III (IONP), IV (IONP +H), V (M-PLL), and VI (M-PLL +H). The stars indicate that the p-values are lower than 10^{-4}.

ACCEPTED MANUSCRIPT

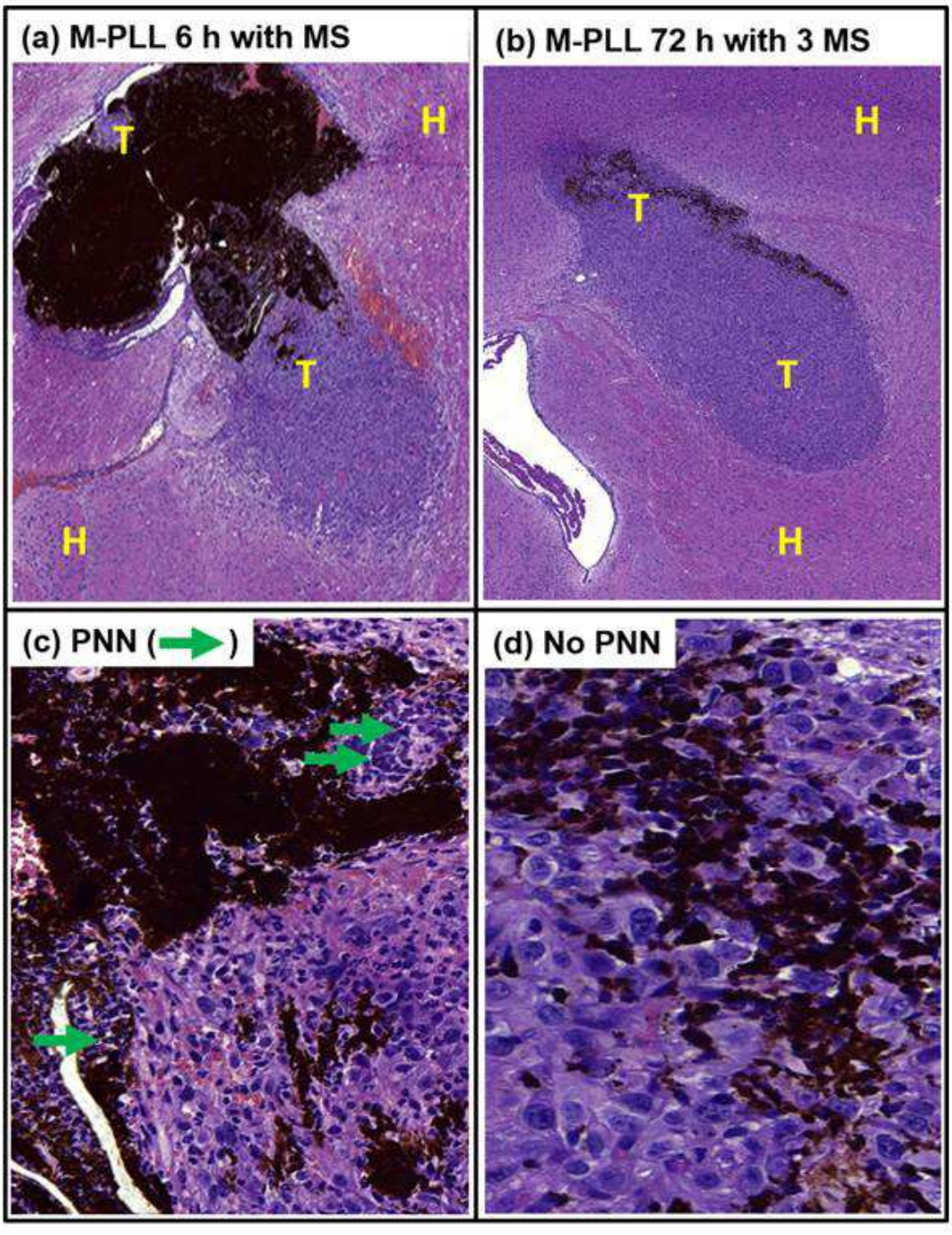


Figure 8

568

569 **Figure 8** Histological optical microscopic images of a brain slide stained with Hematoeosin of a mouse

570 treated by M-PLL intratumor administration followed by one MS (M-PLL 6 h with MS) (a) or by three
571 MS (M-PLL 72 h with 3 MS) (b). (c) and (d) are enlargements of (a) and (b), respectively. In (a) and (b),
572 H and T designate healthy and tumor regions, respectively. The green arrow in (c) points towards
573 polynuclear neutrophils.
574

ACCEPTED MANUSCRIPT

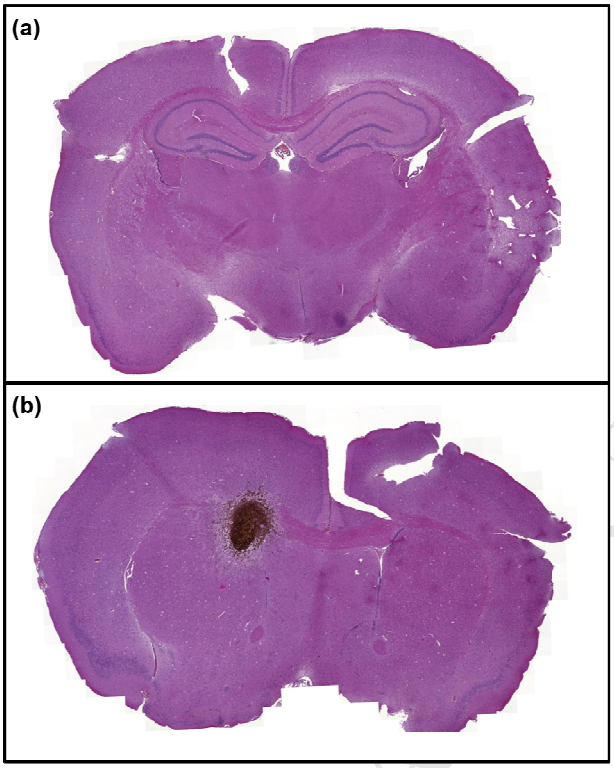


Figure 9 Histological optical microscopic images of a brain slide stained with Hematoeosin, collected from two mice belonging to group VI euthanized 350 days following M-PLL administration, and in some mice, showing the absence (a) or the presence (b) of M-PLL.

ACCEPTED MANUSCRIPT

582 **REFERENCES**

583 [1] Schwartzbaum, J. A.; Fixher, J. L.; Aldape, K. D. et al. Epidemiology and molecular pathology of
584 glioma. *Nature Clinical Practice Neurology* **2006**, *2*, 494-503.

585 [2] Cancer Research UK, Types of primary brain tumours. Last accessed 15 February 2017 [Online]:
586 http://about-cancer.cancerresearchuk.org/about-cancer/brain-tumours/types

587 [3] Ostrom, Q. T. ; Bauchet, L. ; Davis, F. G. et al. The epidiemology of glioma in adults: a ''state of
588 the science'' review. *Neuro-Oncology* **2014**, *16*, 896-913.

589 [4] Stupp, R.; Hegi, M. E.; Mason, W. P. et al. Effects of radiotherapy with concomitant and adjuvant
590 temozolomide versus radiotherapy alone on survival in glioblastoma in a randomized phase III
591 study: 5-year analysis of the EORTC-NCIC trial. *Lancet Oncology* **2009**, *10*, 459-66.

592 [5] Billecke, C.; Finniss, S.; Tahash, L. et al. Polynuclear platinum anticancer drugs are more potent
593 than cisplatin and induce cycle arrest in glioma. *Neuro-Oncology* **2006**, *8*, 215-226.

594 [6] Hashizum,e R. ; Ozawa, T. ; Dinca, E. B. et al. A human brainstem xenograft model enables for
595 bioluminescence imaging. *J. Neurooncol* **2010**, *96*, 151-159.

596 [7] Ross, H. H.; Rahman, M.; Levkoff, L. H. et al. Ethynyldeoxyuridine (EdU) suppresses *in vitro*
597 population expansion and *in vitro* tumor progression of human glioblastoma cells. *J. Neuro-*
598 *Oncology* **2011**, *105*, 485-498.

599 [8] Yang, F. Y. ; Teng, M. C. ; Lu, M. et al. Treating glioblastoma multiforme with selective high-dose
600 liposomal doxorubicin chemotherapy induced by repeated focused ultrasound. *International Journal*
601 *of Nanomedicine* **2012**, *7*, 965-974.

602 [9] Safdie, F.; Brandhorst, S.; Wei, M. et al. Fasting enhances the Response of Glioma to Chemo- and
603 Radiotherapy. *Plos one* **2012**, *7*, e44603.

604 [10] Park, J.K.; Jang, S.J.; Kang, S.W. et al. Establishment of animal model for the analysis of cancer
605 cell metastasis during radiotherapy. *Radiation Oncology* **2012**, *7*, 153.

606 [11] Verhoeff, J. J. C.; Staplers, L. J. A.; Coumou, A. W. et al. Experimental iodine-125 seed
607 irradiation of intracerebral brain tumors in nude mice. *Radiation Oncology* **2007**, *2*, 1-7.

608 [12] Bidwell III, G. L.; Perkins, E.; Hughes, J. et al. Thermally Targeted Delivery of a c-Myc
609 Inhibitory Polypeptide Inhibits Tumor Progression and Extends Survival in a Rat Glioma Model.
610 *Plus one* **2013**, *8*, e55104.

611 [13] Jiang, F.; Zhang, X.; Kalkanis, S. N. et al. Combination Therapy with Antiangiogenic Treatment
612 and Photodynamic Therapy for the Nude Mouse Bearing U87 Glioblastoma. *Photochem Photobiol.*
613 **2008**, *84*, 128-137.

614 [14] Titsworth, W.; Murad G. J. A.; Hoh B. L. et al. Fighting Fire with Fire: The Revival of
615 Thermotherapy for Gliomas. *Anticancer Research* **2014**, *34*, 565-574.

616 [15] Jordan, A.; Scholz, R.; Maier-Hauff, K.; et al. The effect of thermotherapy using magnetic
617 nanoparticles on rat malignant glioma. *Journal of Neuro-Oncology* **2006**, *78*, 7-14.

618 [16] Rabias, I.; Tsitrouli, D.; Karakosta, E.et al. Rapid magnetic heating treatment by highly charged
619 maghemite nanoparticles on Wistar rats exocranial glioma tumors at microliter volume.
620 *Biomicrofluidics* **2010**, *4*, 024111-1.

621 [17] Shinkai, M.; Yanase, M.; Susuki, M. et al. Intracellular hyperthermia for cancer using magnetite
622 cationic liposomes. *Journal of Magnetism and Magnetic Materials* **1999**, *194*, 176-184.

623 [18] Ito, A.; Shinkai, M.; Honda, H. et al. Heat-inducible TNF-α gene therapy combined with
624 hyperthermia using magnetic nanoparticles as a novel tumor-targeted therapy. *Cancer Gene*
625 *Therapy* **2001**, *8*, 649-654.

626 [19] Ohno, T.; Wakabayashi, T.; Takemura, A. et al. Effective solitary hyperthermia treatment of
627 malignant glioma using stick type CMC-magnetite. In vivo study. *Journal of Neuro-Oncology* **2002**,
628 *56*, 233-239.

629 [20] Le, B.; Shinkai, M.; Kitade, T. et al. Preparation of Tumor-Specific Magnetoliposomes and Their
630 Application for Hyperthermia. *Journal of chemical engineering of japan* **2001**, *34*, 66-72.

[21] Maier-Hoff, K.; Rothe, R.; Scholz, R. et al. Intracranial thermotherapy using magnetic nanoparticles combined with external beam radiotherapy: Results of a feasibility study on patients with glioblastoma multiforme. *J. Neuro-Oncology* **2007**, *81*, 53-60.

[22] Maier-Hoff, K.; Ulrich, F.; Nestler, D. et al. Efficacy and safety of intratumoral thermotherapy using magnetic iron-oxide nanoparticles combined with external beam radiotherapy on patients with recurrent glioblastoma multiforme. *J. Neuro-Oncology* **2001**, *103*, 317-324.

[23] Lee, J. H.; Jang, J. T.; Choi, J. S.; Moon, S. H.; Noh, S. H.; Kim J. W.; Kim, J. G.; Kim, I. S.; Park, K. I.; Cheon, J. Exchange-coupled magnetic nanoparticles for efficient heat induction. *Nat. Nanotechnol.* **2011**, *6*, 418-422.

[24] Alphandéry, E.; Lijeour, L.; Lalatonne, Y.; Motte, L. Different signatures between chemically and biologically synthesized. *Sensors and Actuators B: Chemical* **2010**, *147*, 786-790.

[25] Alphandéry, E.; Faure, S.; Seksek, O.; Guyot, F.; Chebbi, I. Chains of magnetosomes extracted from AMB-1 magnetotactic bacteria for application in alternative magnetic field cancer therapy. *ACS Nano* **2011**, *5*, 6279-6296.

[26] Alphandéry, E.; Guyot, F.; Chebbi, I. Preparation of chains of magnetosomes, isolated from Magnetospirillum magneticum strain AMB-1 magnetotactic bacteria, yielding efficient treatment of tumors using magnetic hyperthermia. *Int. J. Pharmaceutics* **2012**, *434*, 444-452.

[27] Alphandéry, E.; Amor, M.; Guyot, F.; Chebbi, I. The effect of iron-chelating agents on Magnetospirillum magneticum strain AMB-1: stimulated growth and magnetosome production and improved magnetosome heating properties. *Appl. Micriol. Biotechnol.* **2012**, *96*, 663-670.

[28] Alphandéry, E.; Faure, S.; Raison, L.; Duguet, E.et al. Heat Production by Bacterial Magnetosomes Exposed to an Oscillating Magnetic field, *J. Phys. Chem. C* **2011**, *115*, 18-22.

[29] Alphandéry, E.; Chebbi, I.; Guyot, F. et al. Use of bacterial magnetosomes in the magnetic hyperthermia treatment of tumours: A review, *Int. J. Hyperthermia* **2013**, *29*, 801-809.

[30] Alphandéry, E. Application of magnetosomes synthesized by magnetotactic bacteria in medicine. *Frontiers in Bioengineering and Biotechnology* **2014**, *2*, 5.

[31] Araujo, A. C. V.; Abreu F.; Silav K. T.; Bazylinski, D. A.; Lins U. Magnetotactic Bacteria as Potential Sources of Bioproducts. *Mar. Drugs.* **2015**, *13*, 389–430.

[32] Bordelon, D. E.; Comejo, C.; Gruttner, C. et al. Magnetic nanoparticle heating efficiency reveals magneto-structural differences when characterized with wide ranging and high amplitude alternating magnetic fields. *Journal of Applied Physics* **2011**, *109*, 124904-1.

[33] Grüttner, C.; Müller, K.; Teller, J. et al. Synthesis and antibody conjugation of magnetic nanoparticles with improved specific power absorption rates for alternating magnetic field cancer therapy. *Journal of Magnetism and Magnetic Materials* **2007**, *311*, 181–186.

[34] MagForce company profile, MagForce AG, The Nanomedicine Company, medical devices for the treatment of brain tumors, last accessed 15 February 2017 [Online]: http://www.magforce.de/en/presse-investoren/aktieninformation/daten-zur-aktie.html

[35] Nanobiotix company profile, NANOBIOTIX HEADQUARTER, last accessed 15 February 2017 [Online]: http://www.nanobiotix.com/_en/about-us/

[36] Dinca, E.B.; Sarkaria, J.N.; Schroeder, M. A.; et al. Bioluminescence monitoring of intracranial glioblastoma xenograft: response to primary and salvage temozolomide therapy. *J. Neurosurg*. **2007**, *107*, 610-616.

[37] Oszkar, S.; Cheryl, B.; Ning, L. et al. Noninvasive Bioluminescence Imaging of Luciferase Expressing Intracranial U87 Xenografts: Corremation with Magnetic Resonance Imaging Determined Tumor Volume and Longitudinal Use in Assessing Tumor Growth and Antiangiogenic Treatment Effect. *Neurosurgery* **2006**, *58*, 365-372.

[38] Zhou, H.; Luby-Phelps, K.; Mickey, B. E. et al. Dynamic Near-Infrared Optical Imaging of 2-Deoxyglucose Uptake by Intracranial Glioma of Athymic Mice. *Plos One* **2009**, *4*, e8051.

[39] Sun, A.; Hou, L.; Prugpichallers, T. et al. Firefly Luciferase-Based Dynamic Bioluminescence Imaging: A Noninvasive Technique to Asszss Tumor Angiogenesis. Neurosurgery 2010, 66, 751-757.

[40] Heitjan, D. F.; Manni, A.; Santen, R. J. Statistical analysis of *in vivo* tumor growth experiments. *Cancer Res.* **1993**, *53*, 6042-6050.

[41] Kim, S. J.; Lee, H.J.; Kim, M.S.; Choi, H.J.; He, J.; Wu, Q. et al., Macitentan, a Dual Endothelin Receptor Antagonist, in Combination with Temozolomide Leads to Glioblastoma Regression and Long-term Survival in Mice. *Clin Cancer Res.* **2015**, *21*, 4630-4641.

[42] Bazylinski, D. A.; Frankel, R. B. Magnetosome formation in prokaryotes. *Nat Rev Micro.* **2004**, *2*, 217-230.

[43] Alphandéry, E.; Perspectives of Breast Cancer Thermotherapies. *J. Cancer* **2014**, *5*, 472-479.

[44] Fischer D.; Li Y.; Ahlemeyer B.; Kriegglstein J.; Kissel T. In vitro cytotoxicity testing of polycations: influence of polymer structure on cell viability and hemolysis. Biomaterials **2003**, *24*, 1121-1131.

[45] Oh Y.; Lee N.; Kang H-W.; Oh J. In vitro study on apoptotic cell death by effective magnetic hyperthermia with chitosan-coated $MnFe_2O_4$. Nanotechnology **2016**, *27*, 115101.

[46] Shetake N. G.; Kumar A.; Gaikwad S.; Ray P.; Desai S.; Ningthounjam R. S.; Kumar J.; Pandey V B N. Magnetic nanoparticle-mediated hyperthermia therapy induces tumour growth inhibition by apoptosis and Hsp90/AKT modulation. Int. J. Hyperthermia **2015**, *31*, 909-9019.

[47] Lin M.; Huang J.; Sha M. Recent advances in nanosized Mn-Zn ferrite magnetic fluid hyperthermia for cancer treatment. J. Nanosci. Nanotechnol. **2014**, *14*, 792-802.

[48] Goya G. F.; Asin L.; Ibarra M. R. Cell death induced by AC magnetic fields and magnetic nanoparticles: Current state and perpective. *Int. J. Hyperthermia* **2013**, *29*, 810-818.

[49] Nikfarjam, M.; Muralidharan, V.; Christophi, C. Mechanisms of Focal Heat Destruction of Liver Tumors. *Journal of Surgical Research* **2005**, *127*, 208-223.

[50] Creixell, M.; Bohórquez, A. C.; Torres-Lugo, M.; Rinaldi, C. EGFR-Targeted Magnetic Nanoparticle Heaters Kill Cancer Cells without a Perceptible Temperature Rise. *ACS Nano* **2011**, *5*, 7124-7133.

[51] Kolaczkowska E.; Kubes, P. Neutrophil recruitment and function in health and inflammation. *Nature Reviews Immunology* **2013**, *13*, 159-175.

ACCEPTED MANUSCRIPT